scientific reports

Check for updates

OPEN

# Demonstration that sublinear dendrites enable linearly non-separable computations

Romain D. Cazé[1,2]✉, Alexandra Tran-Van-Minh[3], Boris S. Gutkin[1,4,6]✉ & David A. DiGregorio[3,5,6]✉

**Theory predicts that nonlinear summation of synaptic potentials within dendrites allows neurons to perform linearly non-separable computations (LNSCs). Using Boolean analysis approaches, we predicted that both supralinear and sublinear synaptic summation could allow single neurons to implement a type of LNSC, the feature binding problem (FBP), which does not require inhibition contrary to the exclusive-or function (XOR). Notably, sublinear dendritic operations enable LNSCs when scattered synaptic activation generates increased somatic spike output. However, experimental demonstrations of scatter-sensitive neuronal computations have not yet been described. Using glutamate uncaging onto cerebellar molecular layer interneurons, we show that scattered synaptic-like activation of dendrites evoked larger compound EPSPs than clustered synaptic activation, generating a higher output spiking probability. Moreover, we also demonstrate that single interneurons can indeed implement the FBP. Using a biophysical model to explore the conditions in which a neuron might be expected to implement the FBP, we establish that sublinear summation is necessary but not sufficient. Other parameters such as the relative sublinearity, the EPSP size, depolarization amplitude relative to action potential threshold, and voltage fluctuations all influence whether the FBP can be performed. Since sublinear synaptic summation is a property of passive dendrites, we expect that many different neuron types can implement LNSCs.**

**Keywords** Synaptic integration, Interneurons, Sublinear dendrites, Feature biding problem

Dendritic filtering influences the shape and amplitude of postsynaptic potentials depending on the synaptic conductance, dendritic morphology, synapse location and the expression of voltage-gated channels[1]. Dendritic properties also influence how multiple synaptic potentials sum, either linearly (if the response amplitude equals the arithmetic sum of the individual synaptic responses), sub-linearly (response amplitude below the sum of the individual responses), or supra-linearly (response amplitude above their sum)[2]. This dendrite-specific arithmetic can greatly enhance a neuron's computational abilities[3] and is thought to be prominent in human neurons[4]. Supra-linear summation is thought to underlie active whisker sensation[5], generate orientation selectivity[6], grid cell activity[7], and sensory perception[8]. In contrast, little is known about the computational advantages imparted by sub-linear dendritic integration[9,10]. Recent computational studies suggest that sub-linear integration in cortical fast-spiking interneurons could contribute to memory encoding[11].

Our previous theoretical work showed that sub- or supra-linear dendritic non-linearities allow a neuron to compute a similar number of functions[12]. For example, for 8 excitatory uncorrelated inputs, a neuron with a sufficient number of non-linear dendrites (either sub- our supra-linear) can implement $10^{17}$ more computations than with purely linear dendritic integration (see methods in[12,13] for details). These additional functions are, by definition, a part of the class of linearly non-separable computations (LNSCs). We should emphasize that both passive sublinear dendrites and active dendritic nonlinearities expand the neurons' computational capacity, albeit under different synaptic placement conditions.

[1]Group for Neural Theory, Laboratoire des Neurosciences Cognitives et Computationelles INSERM U960, Ecole Normale Superieure PSL* University, Paris, France. [2]UMR 8520 CNRS, IEMN, Villeneuve d'Asqu 59650, France. [3]Synapse and Circuit Dynamics Laboratory, Institut Pasteur, Université Paris Cité, CNRS UMR 3571, Paris 75015, France. [4]CCDM, ICN, NRU Higher School of Economics, Moscow, Russia. [5]Department of Physiology and Biophysics, University of Colorado School of Medicine, Anschutz Medical Campus, Denver 80045, USA. [6]These authors jointly supervised this work: Boris S. Gutkin and David A. DiGregorio ✉email: romain.caze@univ-lille.fr; boris.gutkin@gmail.com; david.digregorio@cuanschutz.edu

Our theoretical analysis further predicted that while LNSCs cannot be implemented by a point neuron model, a neuron with sublinear dendrites can robustly implement an LNSC called the feature binding problem (FBP) (Fig. 1). The FBP computation allows a neuron to represent multiple distinct objects, each comprised of independent features. An example of a FBP is given in Fig. 1 where the goal is to detect a yellow circle or a green triangle separately by giving an output of 1, but not respond to a yellow triangle or a green circle (Fig. 1A). This distinction cannot be made by linearly separating the inputs based on their summed amplitudes. Because FBPs are monotone positive Boolean functions (e.g. see[12,13] that can be implemented with only excitatory synapses, we used glutamate uncaging at single synapses to demonstrate this FBP experimentally.

To implement the FBP, supra-linear integration requires that the correct feature conjunction for a given object should synapse onto the same electrical compartment of a dendrite (cluster), while feature conjunctions for subsequent feature combinations signalling other objects would require clustered synapses on other dendrites. In contrast, sublinear integration requires the opposite. Feature conjunctions that should fire the neuron to signal the presence of an object should be scattered on different dendritic segments[1,12]. Thus, the case where scattered inputs fire the cell and clustered inputs do not is essential for solving the FBP using sublinear dendrites (Fig. 1C). Here, we used glutamate uncaging and biophysical modeling to show that the sublinear dendrites of cerebellar molecular layer interneurons render them scatter-sensitive. This, in turn, may enable them to implement the FBP.

## Results

### Cerebellar stellate cells are scatter sensitive

Dendrites of cerebellar stellate cells are thin and integrate synaptic conductances passively[9]. The high-impedance dendrites generate large local depolarization upon excitatory synaptic activation that reduce the driving force for synaptic currents, resulting in a sublinear summation of postsynaptic potentials when activating multiple synapses[14]. Therefore, when synapses on the same sublinear dendrite are activated simultaneously, they "interact" and thus sum less effectively than if synapses were activated on two different dendrites, resulting in a lack of effective electrical interactions. In other words, the somatic depolarization is larger and more sensitive to synapse activation patterns that are "scattered" across the dendritic tree.

We used scanning two-photon glutamate uncaging[14,15] in parasagittal cerebellar brain slices to test the hypothesis that neurons with sublinear dendrites generate larger excitatory potentials when synaptic activation is distributed across dendrites rather than synaptic activation within a dendrite (Fig. 2). We identified stellate cells by patching somata located in the outer third of the molecular layer. To mimic clustered activation, we uncaged glutamate using 0.2 ms 720 nm laser pulses in four locations within putative stellate cell dendritic trees in any one trial (slices were superfused with 2 mM MNI-glutamate) and recorded uncaging-evoked excitatory postsynaptic potentials (uEPSPs) using somatic current clamp patch recordings. Current was injected into the soma to maintain a resting potential near −70 mV. Either all uncaging locations were clustered in the same dendrite, or two uncaging locations were placed on two different primary dendrites (see Fig. 2A). We used pairs of uncaging sites to increase the local depolarization. Compound subthreshold uEPSPs were generated from four sites ranging from 4-22 mV across all experiments (Fig. 2C). For reference, we previously estimated averaged quantal responses elicited midway along the dendrites to evoke 2–3 mV EPSPs[9]. We observed that compound uEPSPs evoked on the same dendritic branch were systematically smaller than their linear sum, as expected for sublinear integration (Fig. 2B,C). However, compound uEPSPs generated from uncaging locations scattered onto two different dendrites were not significantly different than their linear sum and thus consistent with scatter-sensitive subthreshold PSPs. We cannot completely rule out the presence of a small difference between uEPSPs evoked

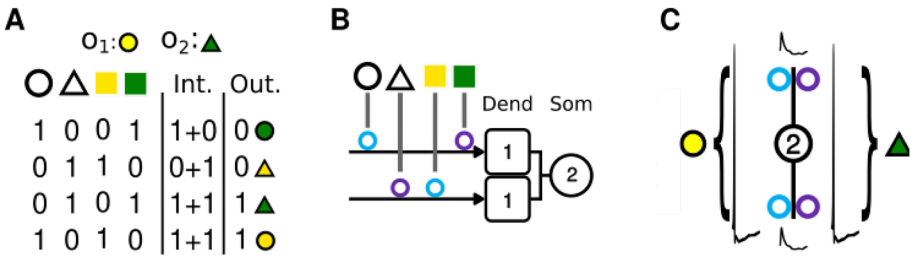


**Figure 1.** The Feature Binding Problem: A linearly non-separable computation and its implementation in a scatter sensitive neuron. (**A**) A truth table describing the FBP of two objects with two features each. The first column describes presynaptic activity: response of a dendrite is active:1 or not:0. The integration column "Int." describes how a neuron's dendrites that implement this computation should integrate inputs. Here we define the dendrite to saturate at 1. Hence for two clustered inputs the response of the dendrites to be integrated at the soma is 1 + 0; for two scattered inputs - it is the arithmetic sum 1+1. The output "Out." column shows if a neuron spikes:1 or not:0. We omit some inputs because whatever the response to them, this computation would still be a LNSC (see "Methods" for more details). (**B**) FBP dendritic implementation: both dendrites must be saturated (saturation threshold of 1 in the square) to trigger the neuron spiking (threshold of 2 in the circle). Because Circle+Green and Triangle+Yellow inputs target the same dendrite, the resulting integration fails to reach the spiking threshold at the soma. Yet for inputs that are scattered soma surpasses its threshold. (**C**) Indicates that the features activating the same dendrites do not reach threshold and cannot generate a spike, but features that are scattered onto the two dendrites generate a somatic spike.

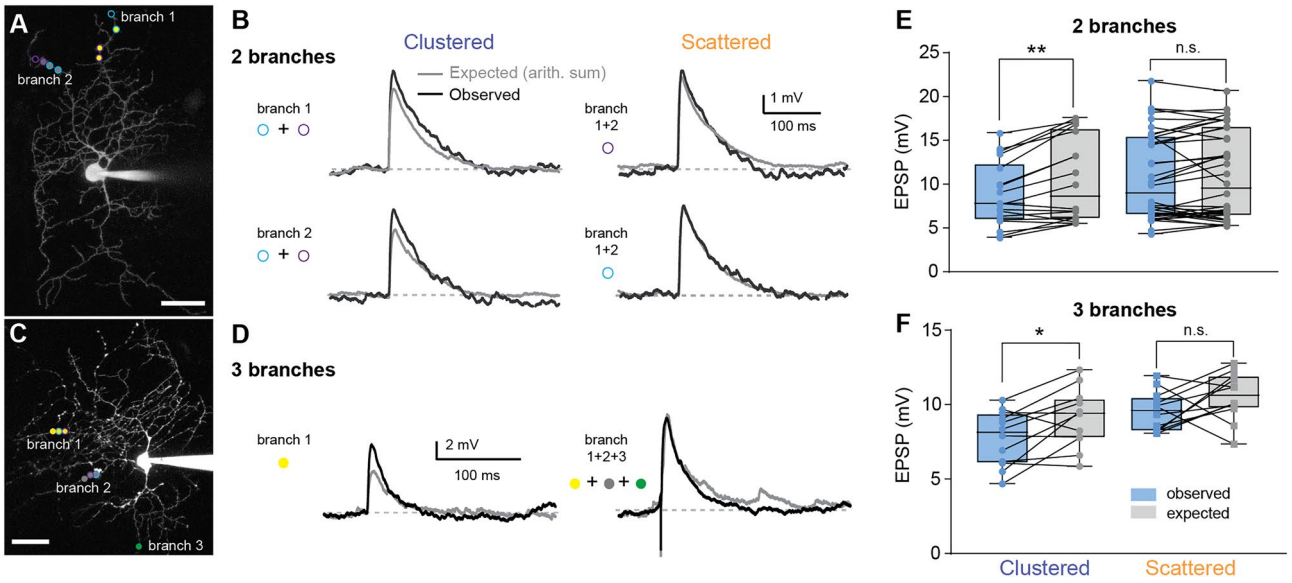


**Figure 2.** Scattered inputs sum more linearly than clustered inputs. (**A**, **C**) 2PLSM image of a cerebellar stellate cell filled with Alexa Fluor 594. Colored spots indicate dendritic locations stimulated using glutamate uncaging (branches 1 and 2, **A** and **C**) or electrical stimulation (branch 3, **C**). The scale bar is 20 $\mu$m. (**B**, **D**) Blue traces are examples of somatic current-clamp recordings in response to uncaging stimulation of two sites on a single dendrite (left) or scattered across multiple dendrites (right). Linear sum of EPSPs recorded in response to uncaging at each individual location gave the "expected" EPSP traces(black traces). (**E**) Peak amplitudes of observed versus expected EPSPs (paired) in response to stimulation of each dendrite pair under clustered or scattered input distributions. A paired Wilcoxon signed-rank test demonstrated that observed responses were statistically smaller than expected $p = 0.002$ (n = 18 for clustered and 38 for scattered; $p = 0.16$ for scattered). (**F**) Similar to E, except three sites per dendritic branch were stimulated. A paired Wilcoxon signed-rank test demonstrated statistically smaller observed responses, $p = 0.003$ (n= 12 for both clustered and scattered, $p = 0.17$ for scattered).

by scattered stimulation and the linear sum that is masked by experimental variability. Nevertheless, the results are consistent with scattered activation generating larger uEPSPs than when equivalent responses are generated by clustered synaptic activation on the same dendrite. Scattered and the clustered glutamate uncaging stimulations were delivered in the same cell. Hence, the comparisons represented by lines in Fig. 2E and F were done for each cell individually.

Next, we increased the number of dendrites tested. However, because of the inertia of galvanometer mirrors, we could more easily perform simultaneous activation of three dendrites if one was stimulated using an extracellular electrode (see "Methods"). Results were similar for the activation of six effective uncaging sites across three dendrites (Fig. 2D–F). These results confirm that compound synaptic potentials in neurons with sublinear dendrites were larger if the inputs were scattered across dendrites rather than clustered on a single dendrite.

Unlike most studies that focus on the characterization of subthreshold dendritic operations, we set out to verify that the scatter-sensitive subthreshold behavior of stellate cell dendrites also translated into scatter-sensitive spiking probability. We applied the same uncaging protocol described for Fig. 2, but adjusted the holding current to maintain the resting potential around −60 mV, to facilitate spiking (NB: while uEPSP amplitudes could not be measured during spiking, we would expect amplitudes on the par with those shown in Fig. 2.) Indeed, we found that, in the same cell, uncaging locations that were on the same dendrite produced a significantly lower spiking probability than when uncaging locations were on separate dendrites (Fig. 3).

These data demonstrate that stellate cells are more likely to fire when inputs of similar size are distributed over their dendritic tree than when they cluster on specific dendrites. We also extended this study to three-branch stimulation as described above and observed a robust increased firing probability if the stimulation was distributed across the dendrites (Fig. 3C,D, and E). Thus, relative to clustered inputs, distributed synaptic input patterns in neurons with sublinear dendrites generate larger EPSPs and higher spiking probabilities, consistent with a scatter-sensitive neuronal computation (i.e. somatic spiking). It remains to be demonstrated that the FBP can be computed by the neuron with scatter-sensitive spike production.

Since we established that stellate cells are scatter-sensitive, we next examined whether such scatter sensitivity would confer the ability to perform linearly non-separable computations. Specifically, we set out to show they could implement the FBP (Fig. 4). Glutamate was uncaged at four distinct locations in six different patterns. There were four scattered cases (uncaging sites on different dendrites) and two clustered cases (uncaging sites on the same dendrite). To observe the possible FBP computation, we examined whether a neuron remained silent (no action potential) in the two clustered cases and fired in two scattered cases with non-overlapping uncaging sites. Let us consider each uncaging location as synaptic input (N.B. potentially a set of converging granule cell synapses) as encoding an object feature. Under this assumption, combinations of uncaging locations that trigger

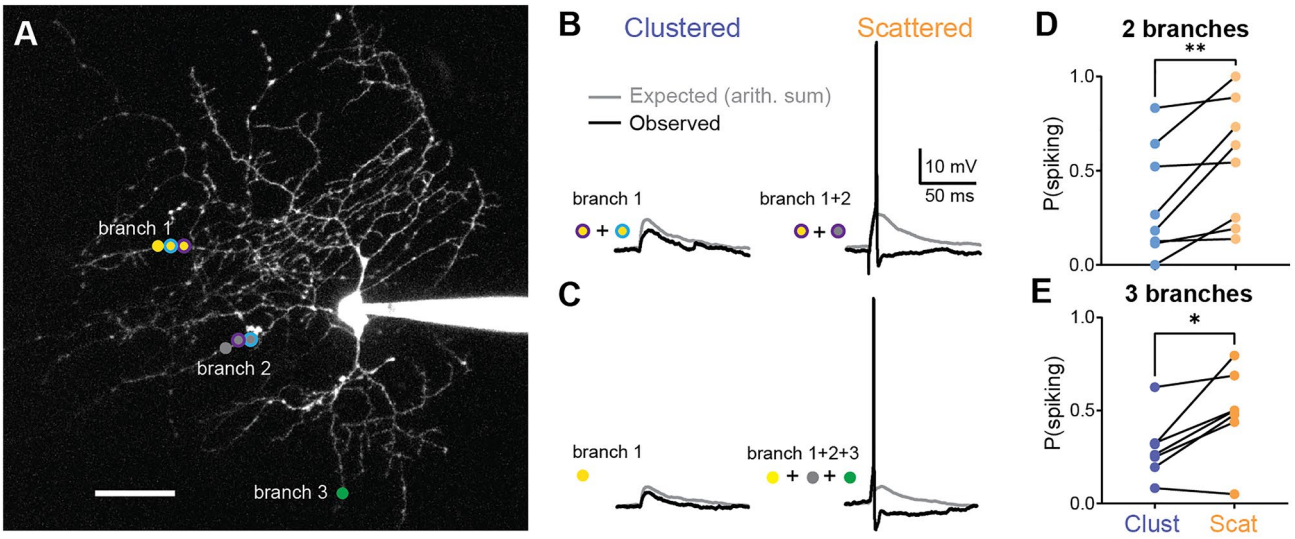


**Figure 3.** Multi-branch glutamate uncaging reveals a higher firing probability for scattered versus clustered stimulation. (**A**) 2PLSM image of a cerebellar stellate cell filled with Alexa Fluor 594. Colored spots indicate locations stimulated using glutamate uncaging (branch 1 and 2) or electrical stimulation (branch 3). The scale bar is 20 $\mu$m. (**B**, **C**) Example traces of somatic current-clamp recordings of electrical responses (EPSPs or APs) to stimulation of a group of clustered (left) or scattered (right) inputs on 2 (**B**) or 3 (**C**) branches. Black traces ("expected") were calculated from the mathematical sum of EPSP responses when the sites were stimulated individually. (**D**) Spike probabilities across cells in response to paired clustered or scattered stimulation within each cell. (**E**) Same as D but when stimulating 3 dendritic branches. A paired Wilcoxon signed-rank test demonstrated a statistically larger spike probability for scattered stimulation in both D and E ($p = 0.01$, n = 8 for stimulation of two branches, $p = 0.03$, n = 7 for stimulation of three branches).

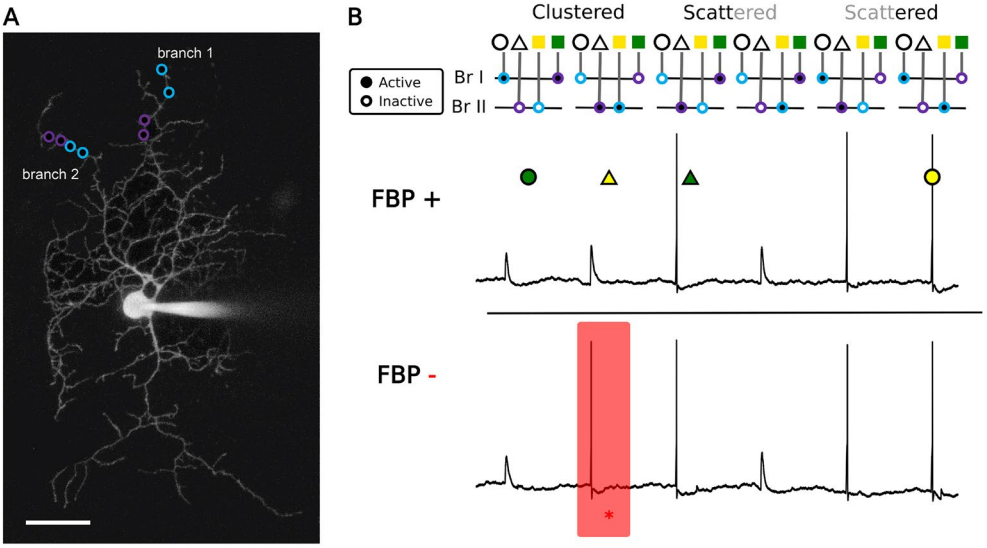


**Figure 4.** Experimental examination of the feature binding problem (FBP) implementation. (**A**) 2PLSM image of a cerebellar stellate cell filled with Alexa Fluor 594. Colored spots indicate the uncaging locations, on this cell we uncaged glutamate in four locations, each pair corresponds to one feature (Purple:"Green" on branch 1, "Triangle" on branch 2; Teal:"Yellow" on branch 2, "Circle" on branch 1). The color code indicates the two objects to be encoded (yellow circle, green triangle). The scale bar is 20 $\mu$m. (**B**) Examples of somatic voltage traces of the same stellate cell in two distinct trials. In the top trial, the neuron computes a feature binding problem, and in the bottom trial it fails because of a false positive (red case). We discarded the two cases when inputs represent the shape or the color inputs only as they do not affect the result. The mean resting potential for this cell was$V_{rest} = -68.5$ mV and estimated variance $\sigma_V = 0.9$ mV, the corresponding histogram of the resting voltage distribution is shown in Fig. 5D.

a somatic spike effectively encode the object. If we observe that the neuron fires for specific combinations of non-overlapping uncaging sites and stays silent for others, then we can claim that its response is compatible with the neuron implementing the FBP.

To give a proof-of-principle demonstration, we labelled each uncaging location with a unique feature symbol shape or color: a triangle or a circle shape, and green vs. yellow color. The feature binding problem is correctly implemented if the objects "green triangle" and "yellow circle" were encoded by spiking at the soma, while other combinations did not lead to spiking. Experiments showed multiple trials in which the results were consistent with the FBP, while in others they were not (either scattered synaptic activation did not produce a spike or the clustered case did) (see Fig. 4 lower right, red shading). The cell shown in Fig. 4 showed responses compatible with it implementing the FBP in nearly half of the trials (n = 15, with each trial consisting of all 6 relevant stimulation combinations), i.e. it fired for two objects with two specific disjoint features (e.g. green triangle or yellow circle) and stayed silent for two other objects made up of other disjoint feature combinations (the green circle and yellow triangle). In this cell, we also observed trials where a false positive spike was generated (red shading Fig. 4). Because of the costly experimental setup, we performed supra-threshold experiments only on four cells, where we stimulated a couple of dendrites. Two cells were capable of implementing the FBP 50% of the time. We used a realistic biophysical model to strengthen this experimental work and explain cases where cells fail to implement the FBP.

## Scatter sensitivity is necessary but not sufficient for the feature binding problem implementation with passive dendrites

To understand better the origin of the failed FBP trials, we implemented a biophysical model of a cerebellar stellate cell. We built a multi-compartment model with a realistic dendritic tree morphology (using a reconstruction of cerebellar stellate cell[16]) that was capable of reproducing the uEPSP amplitudes observed in the subthreshold protocol (see Fig. 5, 4 pS peak synaptic conductance). The dendrites were modeled as passive and showed sublinear EPSP summation with clustered inputs and more linear summation with inputs scattered on different dendrites (Fig. 5A and B). Spikes we generated by an integrate-and-fire mechanism with the firing threshold of −50 mV (see "Methods"). Using preliminary simulations of a reduced "ball-and-stick" model, we found that there was an optimal soma-to-stimulated-location distance that maximizes the sublinear summation of EPSPs of the clustered inputs thus generating a large difference between clustered and distributed inputs and optimizing scatter sensitive computations (Supplementary Materials, see Supplementary Fig 1). We, therefore, used these results as a guide to place the simulated stimulation locations on the model dendritic tree.

We considered two principal factors that could underlie trial-to-trial and cell variability, and thereby affect the ability to implement the FBP: the EPSP size relative to the threshold and membrane fluctuations. To correctly implement the FBP, the single uEPSP and the sublinear compound uEPSP (two-site activation within the same dendrite) must be subthreshold and the linearly summed uEPSPs (two-site activation on different dendrites) must be supra-threshold. We thus varied the resting membrane voltage and examined if simulated compound uEPSPs (adjusted to 10 pS per site to ensure spikes) produced false positive or negative spikes (compare Fig. 5 to Fig. 4). For the depolarized resting membrane potential of −64 mV, the model reaches the threshold not only in all the scattered stimulation cases but also in one of the clustered cases, creating a false positive. When the membrane potential was decreased to −68 mV, the model neuron reached the threshold only in the scattered case, thus correctly implementing the FBP. Finally, if the resting membrane potential was set too low (−72 mV), the neuron spiked only in one of the scattered cases. Together, these three simulations demonstrate that variations in the resting membrane voltage can influence a successful FBP computation. Moreover, the EPSP size relative to the threshold must be tuned appropriately to implement the FBP correctly.

We also recognized that membrane potential fluctuations could generate false positives and false negatives. We, therefore, modeled the voltage fluctuations using a Gaussian noise distribution that matched experimental observations (mode at −68.4 mV with a standard deviation equal to 0.9 mV). We, therefore, systematically varied the noise level around this experimental value as well as varying the resting membrane potential of the model from −72 mV and −64 mV (Fig. 5E). To calculate the FBP probability, we performed 1000 trials for each simulation condition. As expected from above, when the resting membrane potential is too high, the neuron generated false positive spikes, and when it is too low, the neuron generated false negatives. The simulations indicated an optimum around a resting membrane potential of -68 mV, but the FBP probability degraded within increasing membrane potential fluctuations.

These simulations show that for a particular dendrite input impedance (dendrite diameter), there are specific ranges of synaptic conductances, amplitude of the firing threshold above baseline, and noise levels that influence the probability of implementing the FBP. We showed the simulation parameters in which we match the 50% observed for a representative cell, Fig. 4. We, therefore, conclude that scatter-sensitive neurons can perform the FBP, but the relative amplitude of the EPSP versus the voltage-to-threshold and the membrane fluctuations need to be tuned to compute the FBP reliably.

## Simulating the experimental trial to trial variability of the feature binding problem implementation for a single stellate cell

To demonstrate that sublinear dendrites can indeed perform the FBP even in noisy experimental conditions, we simulated the trial-to-trial variability observed experimentally by simulating the experimental membrane voltage fluctuations, EPSP and observed threshold of the cell shown in Fig. 4 (Fig. 6); see "Methods" for description of the noise generation procedure that matched the resting voltage distribution of the model with the cell shown in Fig. 6B). For this cell, the experimental voltage fluctuations resulted in a mean resting potential of -68.3 mV and SD of 0.9 mV (Fig. 5D)) when visually fitted with a Gaussian function. These statistics were matched

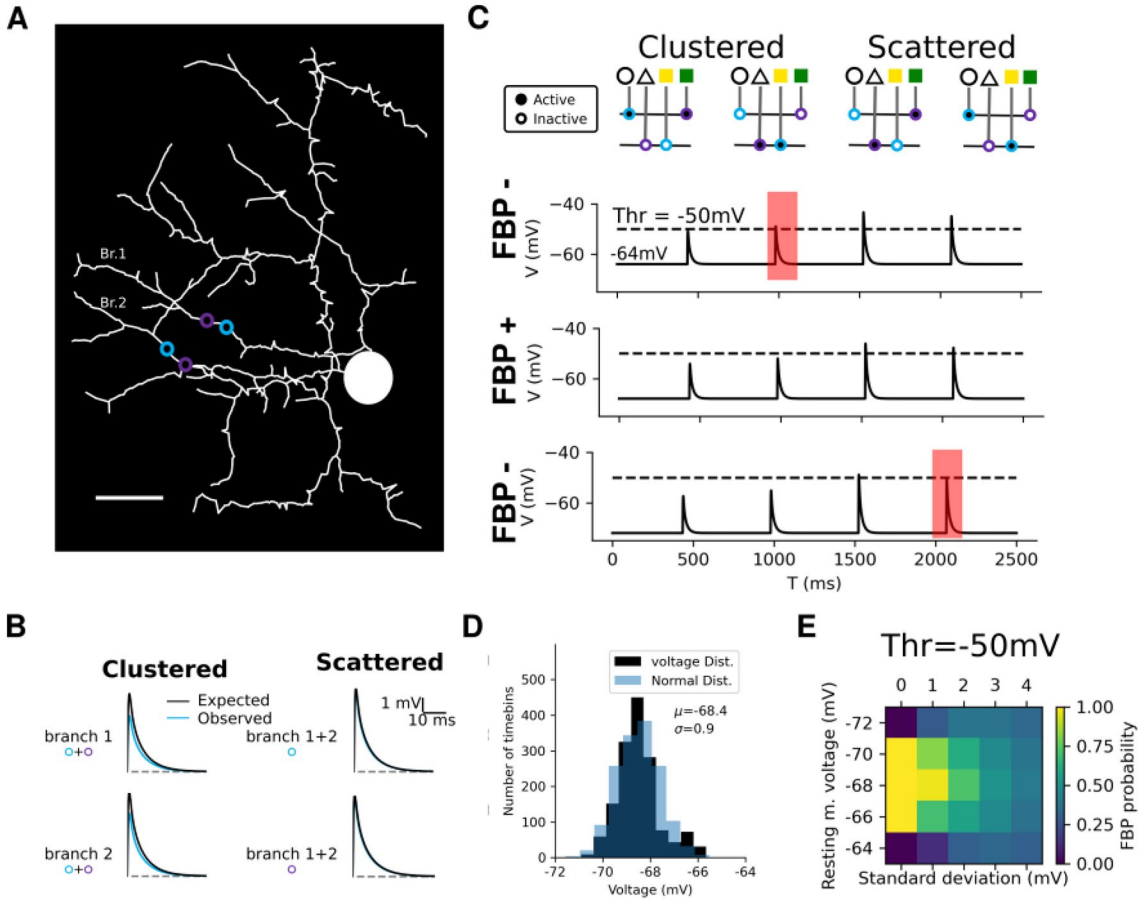


**Figure 5.** Simulations exploring synaptic and cell parameters necessary to perform FBP. (**A**) Morphologically detailed model of a cerebellar stellate cell. Colored circles indicate input locations corresponding to the two combinations of features (teal: yellow + circle; purple: green+triangle. The scale bar is 20 $\mu$m. (**B**) compound uEPSPs were simulated by placing two 4 pS synaptic conductances (max value) with a $\tau = 1$ ms time constant on the same (clustered) or different dendrites (scattered). (**C**) The diagram indicates the membrane potential responses for compound uEPSP responses when stimulating pairs of uncaging locations. The dashed line indicates the spiking threshold (threshold V $= -50$ mV, see "Methods" for further details) . Note that only a resting membrane potential of – 68 mV allows for a correct implementation of the FBP, the two other voltages lead to errors in the FBP implementation- being due to respectively a false positive (extraneous spike) and a false negative (absence of a spike). (**D**) Histogram of the experimental voltage distribution (black, we used the first 300 ms without spikes and measured the mean voltage in 2 ms time bins) follows a normal-like distribution ($\mu_V = -68.5$ mV, $\sigma_V$=0.9 mV; light blue superimposed). (**E**) The probability of implementing the FBP for different resting membrane potentials and noise levels (SD), calculated from 1000 simulations for each condition.

by the model. Our data-adjusted model simulation reproduced the observed FBP probability (Fig. 6A–C top) of approximately 50 percent (Fig. 6A–C bottom). As we see in our simulations, like the experimental recording, our model also failed to implement the FBP in certain trials because its resting membrane voltage fluctuate randomly (Fig. 6B). We note that the model further matched the error trials in the neuron, giving spurious spikes at the inputs encoding the yellow triangle (Fig. 6C). This enabled us to simulate the variability observed experimentally (Fig. 6C). Like the experiment, this simulated neuron implemented the FBP in seven trials over fifteen. More generally, out of the 13 neurons to which we subjected this protocol, we observed 7 cells that generated at least two successful FBP trials, of which two cells implemented the FBP with a probability of close to 0.5.

In Fig. 6, we used the same biophysical model as described above with four synaptic inputs (i.e. glutamate uncaging sites) placed as indicated in Fig. 5A with peak amplitudes of Branch 1 (Br1) teal:7 pS, purple:3 pS; Branch 2 (Br2) teal:20 pS, and purple:10 pS, to match as close as possible the experimental data. The two first stimulation points have a weaker value than the two last, as the second uEPSP is larger than the first. The third input guarantees that the neuron will fire in the third scattered case (20 + 3 pS), while the sum is lower in the second scattered case (10 + 7 pS) keeping the neuron silent in this situation. Thus this model could reproduce experimental observations (Fig. 6A).

Furthermore, we noticed that when the neuron failed to perform the FBP consistently, this was due to false positive spikes ("yellow-triangle" combination in Fig. 6C, marked with the red arrow). To examine why the

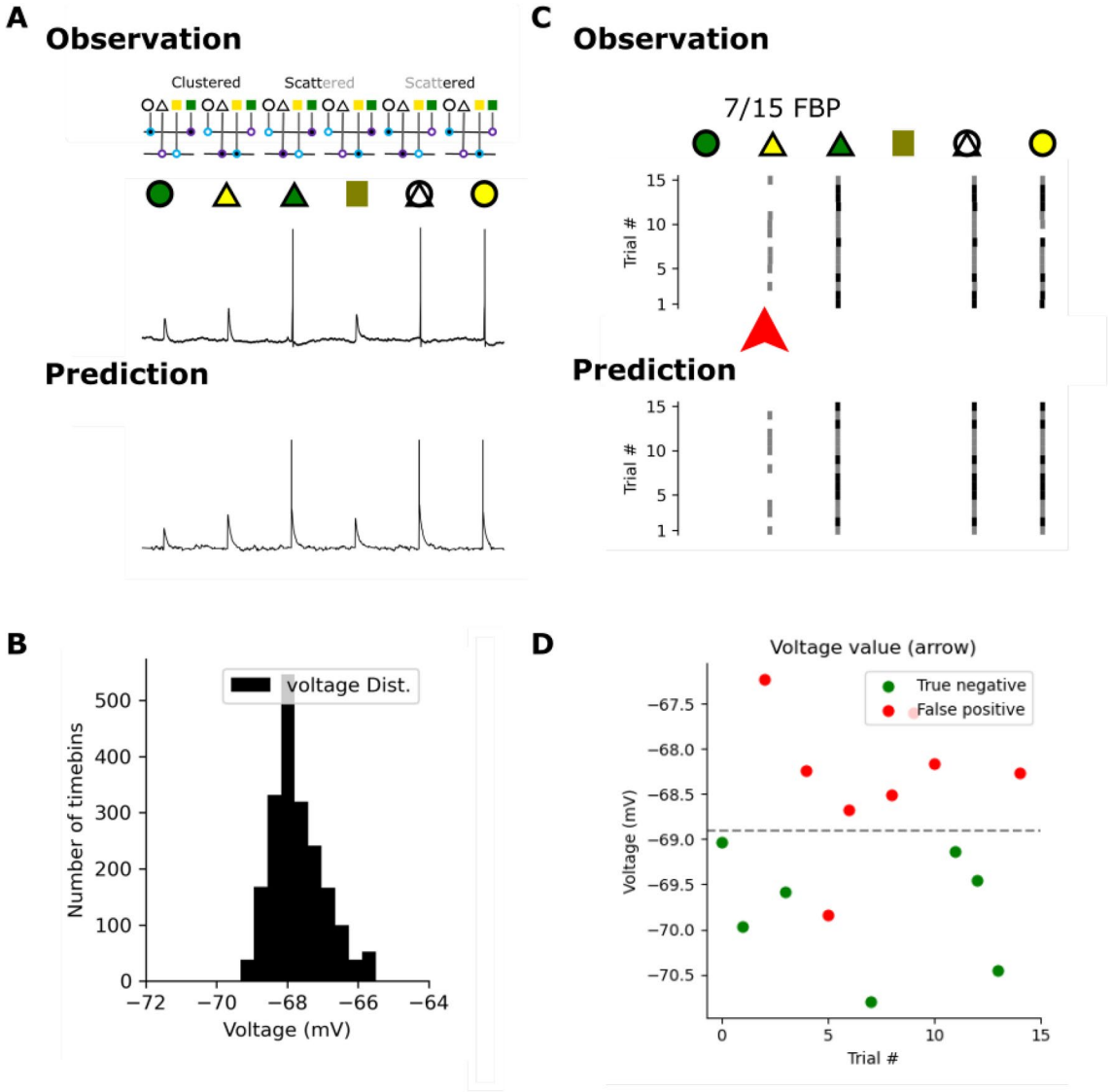


**Figure 6.** Model simulations with realistic parameters reproduce measured FBP probability. (**A**) Top, single trial somatic voltage trace recorded from a cerebellar stellate cell in response to uncaging stimulation patterns as shown in Figs. 4 and 5. Bottom: a simulated voltage trace with when a 4 ps conductance change was implemented in model SC with realistic dendritic tree and membrane potential fluctuations. Importantly, the simulation reproduced the successful FBP of the experiment. (**B**) voltage fluctuation histogram for the resting potential estimated from quiescent periods of the simulated trace (2ms histogram time bins) to mimic the experimental histogram in Fig. 5D (**C**) Spike times for experimental and simulated traces. Trials in black are those in which the FBP was correctly implemented, showing a similarity between experiment and simulations. (**D**) Values of the recorded membrane voltage 10 ms before the stimulation episode marked with the red arrow in panel (**C**), colored in green when the neuron stays silent and in red when the neuron spikes. Spikes, in this case, correspond to false positives. The dashed line is for illustration purposes and separates the two responses.

neuron fails to perform the FBP in these specific trials, we plotted the membrane voltage of the cell just before the stimulation (10 ms before; see Fig. 6D), and we colored each point depending on the cell response (spikes:red, silence:green). The resting potential for trials where a neuron gave a false positive spike was significantly depolarized. This led to consistent failure to implement the FBP (14 cases out of 15). While for correct negatives, the resting potential was hyperpolarised. This supports our conclusion that the probability of implementing the FBP depends on the resting potential just before the response. The resting potential fluctuations, on the other hand, also lead to the FBP implementation failures in some trials but not others.

## Discussion

Dendritic nonlinearities can theoretically increase the computational capacity of neurons because they enable multi-layered information processing. In particular, while there has been fast-growing theoretical literature arguing for universal computing power of dendritic neurons[3,11,12,17] (bolstered by experimental results on subthreshold

dendritic integration[1,2,4,5] and the potential role of dendritic processes in neuronal tuning properties[8,18–20]), experimental validation of an actual implementation of LNSC by a neuron endowed with nonlinear dendrites, to our knowledge, has not been performed. In this study, we demonstrated using multi-point glutamate uncaging that the sublinear dendritic integration of cerebellar stellate cells leads to larger EPSPs and spiking probabilities when synaptic activation is spread across dendrites (scatter-sensitive) as compared to when the synapses are activated within the same dendritic branch. We also provided evidence that stellate cells can implement the FBP (as previously predicted in[12]).

Unlike non-monotone LNSCs (e.g., the exclusive-or function, XOR) the FBP can be computed using only excitatory synapses. This property of the FBP allowed it to be demonstrated experimentally with glutamate uncaging. On the other hand, demonstrating XOR-like computations would require a mixture of caged neurotransmitters or a non-monotone input-output transfer function that has not been observed in cerebellar stellate cells. Moreover, the FBP is of particular interest since neurons implementing it are able to bind multiple feature combinations together into an object[21,22]. Finally, modeling dendritic integration of the thin passive dendrites of cerebellar stellate cells allowed us to identify the biophysical conditions necessary to perform this benchmark.

We have shown here that in order to implement the FBP using excitatory synapses and sublinear dendrites, the two features of a common object have to innervate two different dendrites such that their compound EPSP, upon simultaneous activation, is maximized and generates the large spike probability. Otherwise, if two synapses are simultaneously activated within the same dendritic compartment, and their summed local depolarization is large enough to decrease the driving force for ionic currents, the net somatic depolarization will be smaller than the arithmetic sum. Thus, clustered synaptic activation produces less depolarization than when the synapses are electronically independent. For a neuron to bind two (or more) features of an object, the features must be distributed across the dendritic tree to maximize the spike probability associated with the object, a computation termed "scatter-sensitive". Hence, an important condition for a single neuron to implement the FBP is that the scattered activation produces a somatic spike, whereas the equivalent clustered activation must be subthreshold for spike generation. This fine-tuning requires a specific relationship between the EPSP amplitude, the number of synapses associated with each feature and the different features, and the difference between the resting membrane potential and the spike threshold. EPSPs that are too strong generate false positives, whereas EPSPs that are too weak generate false negatives, spiking representations of objects (Fig. 5). Stronger background membrane potential fluctuations will also generate more false positives and negatives on a trial-to-trial basis (see Figs. 4 and 6).

In this study, we emphasized the scatter-sensitivity of the neuron as a key factor for the implementation of linearly non-separable computations, as it is possible both in active and passive dendrites. Passive thin dendrites have high input impedances and are good candidates for large local depolarizations that generate sublinear summation. Activation of voltage-gated potassium conductances can also generate sublinear integration[10]. Moreover, it is possible that for small numbers of active synapses, their compound EPSP can be large enough to decrease the driving force locally in the dendrite but still too small to activate nonlinear conductances[23]. In that window of synaptic depolarization, a scatter-sensitive computation can be performed. Moreover, for dendrites that exhibit robust calcium spikes[9], once the dendritic spike has been generated, additional synaptic depolarization is ineffective in increasing spike probability. Synaptic contacts scattered onto other dendrites must be activated to generate additional somatic depolarization and increased spike probability. Thus, both interneurons and principal neurons could exhibit scatter sensitivity and thus use sublinear summation to implement a LNSC[11], albeit under specific regimes of synaptic and intrinsic cell membrane parameters.

For technical reasons, we tacitly used a minimal number of synaptic inputs, assuming each had one input per feature, that we distributed across two dendritic segments to demonstrate that the cellular spiking response was compatible with the FBP computation. This, of course, is only a minimal proof-of-principle configuration. A given feature may indeed be represented by a set of multiple synaptic inputs emanating from a number of presynaptic neurons, converging onto a given dendritic segment (or an electrotonically compact subset of the dendritic tree) and co-activated to signal that feature being present. Such convergence is likely for the cerebellar circuitry, as there is a nearly 1:300 expansion ratio between Mossy-fiber inputs and granule cells (which form synapses onto molecular layer interneurons and Purkinje cells). Thus, a single feature can be easily encoded by multiple GCs due to redundancy. For the bound object, to be signaled by the somatic spiking, synpases conveying common features would need to be located at electrotonically large distances from each other. Monitoring such complex spatiotemporal dendritic dynamics is a formidable future challenge, requiring additional experiments and biophysical modeling.

An caveat of our work is that we focused on a proof-of-principle demonstration that a neuron with sublinear dendrites an implement the FBP as it is defined mathematically (as per the truth table in Fig. 1). This definition leaves responses to certain scattered "non-object" combinations of features ambiguous (see the full FBP truth table in "Methods") without negating our demonstration. However, from a neural coding point of view, it would be preferential that our dendritic neurons fire only to object feature combinations. In other words, neurons spike exclusively to the "green triangle" and/or "yellow circle". While such exclusive spiking is implementable in a straight-forward way with supra-linear dendrites, it is conceivable such an "exclusive object signaling" function may be possible to implement with sublinear dendrites by encoding the object features with specific EPSP amplitudes relative to the spiking threshold. Thus, the biophysical mechanisms (synaptic- and dendritic- or circuit-based) underlying FBP implementation remain a critical subject for future work.

Another shortcoming of using sublinear dendrites to implement FBP[12,13], is that the number of required sublinear dendritic segments tends to grow with number of objects and/or object features. This growth is linear for supralinear dendrites and exponential for passive dendrites. Hence, we would speculate that sublinear dendrites best sub-serve low-dimensional LNSCs. Yet despite these caveats, given that scatter sensitivity responses on passive cable properties of dendritic trees and is not catastrophically deteriorated by active dendritic processes

(albeit under different synaptic and intrinsic regimes), it might be a generic property of information processing in many classes of neurons.

## Methods

### Animals and slice preparation

Animal experiments were performed in accordance with the guidelines of Institut Pasteur, France, and all protocols were approved by the Ethics Committee 89 of Institut Pasteur (CETEA; approval DHA180006). Results of this study are reported in accordance with ARRIVE guidelines (https://arriveguidelines.org).

Cerebellar acute slices were prepared from CB6F1 mice (F1 cross of BalbC and C57Bl/6J) on postnatal days P60 to 90. The mice were killed by rapid decapitation (no anesthetic was used), after which the brains were quickly removed and placed in an ice-cold solution containing (in mM): 2.5 KCl, 0.5 CaCl2, 4 MgCl2, 1.25 NaH2PO4, 24 NaHCO3, 25 glucose, 230 sucrose, and 0.5 ascorbic acid bubbled with 95% O2 and 5% CO2. Parasagittal slices (20 0$\mu$m thick) were prepared from the dissected cerebellar vermis using a Leica VT1200S vibratome. After preparation, the slices were incubated at 32 degrees Celsius for 30 minutes in the following solution (in mM): 85 NaCl, 2.5 KCl, 0.5 CaCl2, 4 MgCl2, 1.25 NaH2PO4, 24 NaHCO3, 25 glucose, 75 sucrose and 0.5 ascorbic acid. Slices were then transferred to an external recording solution containing (in mM): 125 NaCl, 2.5 KCl, 2 CaCl2, 1 MgCl2, 1.25 NaH2PO4, 25 NaHCO3, 25 glucose and 0.5 ascorbic acid, bubbled with 95% O2 and 5% CO2, and maintained at room temperature for up to 7 hours.

### Slice electrophysiology and imaging

Whole-cell current-clamp recordings were performed from stellate cells (SCs) (33°C–36°C) located in the outer third of the molecular layer, using a Multiclamp 700B amplifier (Molecular Devices), and fire-polished thick-walled glass patch-electrodes (tip resistances of 4-6 MΩ). The pipettes were backfilled with an internal solution containing (in mM): 110 K-MeSO3, 40 HEPES, 1 EGTA, 4.5 MgCl2, 0.49 CaCl2, 10 Na-pyruvic acid, 0.3 NaGTP, 4 NaATP, 10 Tris phosphocreatine and 0.04 Alexa Fluor 594 and adjusted to 305 mOsm and pH 7.3. Synaptic responses were filtered at 10 kHz and digitized at 100 kHz using an analog-to-digital converter (model NI USB 6259, National Instruments, USA) and acquired with NClamp (www.neuromatic.thinkrandom.com), running in the Igor Pro environment (Wavemetrics). Current was injected to maintain the membrane potential between −70 mV and −90 mV (after correcting for liquid junction potentials, calculated to be −7 mV using JPCalcW (Barry, 1994; J. Neurosci. Method., 51: 107–116)), and series resistance was compensated by balancing the bridge and compensating pipette capacitance.

Unless otherwise stated, the external solution included 10 $\mu$M SR-95531 to block GABAA receptors to avoid confounding results due to partial blockade of GABAA receptors by MNI glutamate, and 50 $\mu$M D-AP5 to avoid stimulation of extra-synaptic NMDA receptors.

A pulsed Ti: Sapphire laser (DeepSee, Spectra-Physics) beam tuned at 810 nm was scanned on the preparation using an Ultima microscope (Bruker Fluorescence Microscopy) mounted on an Olympus BX61WI microscope and equipped with a 60× (1.1 NA) water-immersion objective. Simultaneous two-photon fluorescence and Dodt contrast imaging (Luigs and Neumann, Germany) were used to position extracellular stimulating electrodes and uncaging points along spatially isolated dendrites of Alexa Fluor-594-filled SCs, using a transmitted light PMT mounted after the Dodt tube to acquire a laser-illuminated contrast image simultaneously with the 2PLSM image. Alexa Fluor 594 fluorescence was filtered using 640/100 nm bandpass filters (Chroma) and detected using side-on multi-alkali PMTs (3896, Hamamatsu Photonics). In addition to the light collected through the objective, the transmitted infrared light was collected through a 1.4 NA oil-immersion condenser (Olympus), and reflected on a set of substage photomultiplier tubes (PMTs).

### Chemicals

D-AP5 (D-(-)-2-Amino-5-phosphonopentanoic acid) and SR 95531 (2-(3-Carboxypropyl)-3-amino-6-(4 methoxyphenyl) pyridazinium bromide) were purchased from Abcam, UK. MNI-glutamate (4 methoxy-7-nitroindolinyl caged L-glutamate) was purchased from Tocris Bioscience, UK. Alexa Fluor 594 was from Life Technologies, USA. All other chemicals were purchased from Sigma-Aldrich, France.

### Glutamate uncaging

MNI-glutamate was bath-applied at a final concentration of 2 mM in ACSF, and recycled. The solution was kept protected from light, and all lamps used for ambient light and microscope trans-illumination were covered with a UV yellow filter to prevent undesired photolysis of MNI-glutamate. The preparation was illuminated through a second set of galvanometer-based scan mirrors, allowing independent and rapid positioning of the photolysis beam. The photolysis laser was a pulsed Ti:Sapphire laser (DeepSee, Spectra-Physics) tuned at 720nm. The outputs of the two lasers were independently modulated to combine uncaging of MNI-glutamate and imaging morphology. The imaging laser beam was modulated using a Pockels cell (350-50-BK 02, Conoptics, Danbury, CT). For two-photon uncaging, the intensity and duration (200-300 $\mu$s) of the photolysis pulse was modulated using an acousto-optic modulator (MT110-B50A1.5-IR-Hk, AA Opto-Electronic, France). A telescope placed on the path of each uncaging beam (Thorlabs) was used to adjust the convergence angle to both backfill the objective and match the focal plane of the two-photon excitation for imaging. Parfocality of the two beams was verified using bleached spots on a microscope slide coated with fluorescent ink. Photolysis laser powers, estimated at the exit of the objective, were <1 mW for 1P uncaging and <20 mW for two-photon uncaging. We uncaged near simultaneously at up to 6 spots, each 3–6 $\mu$m apart, by rapidly switching the focal spot to each new location along the dendrite at 200 $\mu$s intervals. Dendrite diameters were characterized thoroughly in[9], which were nearly always less than 0.5 um, with a mean of 0.4 um. For multi-dendrite stimulations, the minimum displacement

time of uncaging mirrors between two uncaging locations constrained the path distance between the stimulated dendrites (typically on the order of 100-150 $\mu$m between the most distant uncaging locations). Each uncaging pattern was elicited over 10-20 trials and then averaged to obtain an accurate estimate of response amplitudes.

## Distribution of the resting membrane voltage

The voltage membrane was simulated with step sizes of 1 ms. We looked at all 15 trials and used the first 100 ms to plot a histogram of the voltage distribution. We have overlapped surrogate data (n = 150000 points) generated from a normal distribution using the observed $\mu = -68.48$ mV and $\sigma = 0.90$ mV. We used a visual comparison to a Gaussian function to test the normality of the distribution.

## Formal definition of the FBP

The definition of the FBP in Table 1 ensures that FBP is positive (therefore monotone) and linearly non-separable. Previously, we proved using constructive proof that a neuron with a sufficient number of sub or supra-linear subunits could compute all positive functions[13]. In the same paper, we showed that the number of required non-linear subunits scales linearly for supra-linearity and exponentially with sub-linearity.

It is important to note here that the FBP is a monotone function, contrary to the XOR, and can be experimentally tested with only excitatory caged neurotransmitters.

Here we focus on the simplest FBP (2 objects and 4 features, each object made up of 2 specific features). This choice is motivated by experimental constraints as we found that fast glutamate uncaging beyond 2 locations was technically not feasible.

## Biophysical model

All simulations were performed with Brian 2[24] and we used a detailed reconstruction from[16]. The code needed to reproduce the relevant figures is available under an open-source license at https://doi.org/10.5281/ZENODO.7875425. We used a conductance-based model with the reconstructed dendritic arbor. The axial resistance between compartments equals 150 Ω. Every compartment contained the following passive currents:

$$C_m \frac{dV}{dt} = g_L(V - E_L) + I_s \tag{1}$$

$V$ is the membrane potential, $C_m = 1\,\mu\text{F cm}^{-2}$ is the membrane capacitance, $g_L$ is the leak capacitance equal to $5e-5$ Siemens which is equivalent to an input resistance of, $R_i = 20000\Omega$.

The synaptic current $I_s$ is described by

$$I_s = g_s(E_s - V) \tag{2}$$

with $E_s$ being the synaptic reversal potential and $g_s$ the synaptic conductance. This conductance jumps up instantaneously for each incoming input and decays exponentially with a time constant $\tau_s = 1$ ms, otherwise:

$$\frac{dg_s}{dt} = -\frac{g_s}{\tau_s} \tag{3}$$

Because our study focused on subthreshold synaptic integration leading up to spiking, we generated spikes with a simple integrate-and-fire mechanism and considered that a neuron emits a spike when the somatic voltage crosses a given threshold set at -50 mVs. This is further justified by the fact that glutamate uncaging elicited brief EPSP-like depolarizations and the evoked action potentials in the cerebellar stellate cells exhibit a very sharp onset and appear to be all-or-none.

## Simulations to match the experimental observation

In Fig. 6 we used the same biophysical model as described above with four synaptic conductances placed as indicated (Fig. 6A) with peak amplitudes of Br1 teal:7 pS, purple:3 pS; Br2 teal:20 pS, and purple:10 pS exponentially decaying with a 1 ms time constant, to match as close as possible the experimental data (uEPSP amplitude or spike probability). The first two stimulation points have a weaker value than the last two, since the second uEPSP is larger than the first. The third input with a high value guarantees that the neuron will fire in the third scattered case (20 + 3 pS) while the sum is lower in the second scattered case (10 + 7 pS), keeping the neuron silent in this situation.

To mimic the observed variation in the membrane resting voltage, we used a dual-conductances based process, one inhibitory and one excitatory of 0.2 pS targeting the soma. To create randomly distributed membrane

| In | 0000 | 0001 | 0010 | 0100 | 1000 | 1001 | 0110 | 0101 | 1010 | 0011 | 1100 | 1110 | 1101 | 1011 | 0111 | 1111 |
|---|---|---|---|---|---|---|---|---|---|---|---|---|---|---|---|---|
| Out | 0 | 0 | 0 | 0 | 0 | 1 | 1 | 0 | 0 | *?* | *?* | 1 | 1 | 1 | 1 | 1 |

**Table 1.** The FBP truth table organised depending on the number of 1s in the input vectors (the In row). For input vectors with less than two 1s the neuron should stay silent, and if it has more than two 1s the neuron should fire. When there are two 1s, the neuron should fire for two disjoint conjunctions and stay silent for two of other disjoint conjunctions. This guarantees that the FBP is a LNSC. In the two other cases the neuron could fire or not (as marked by *?*).

voltage in the model, we used the following procedure. We randomly picked 400 integers between 0 and 2000, each with the same probability. Of these, 200 corresponded to the times at which an excitatory synapse activates (with the reversal potential of 0 mV) and the other 200 to the activation times of an inhibitory synapse (reversal potential −140 mV). Both of these surrogate synapses target the soma and have a conductance strength of 0.2 nS. Each synapse was modeled as an instantaneous increase preceding an exponential decay with a 1ms time constant. The goal was to obtain a resting potential distribution that matched the experimentally observed one (see Fig. 6A).

The Python code to entirely reproduce the two last figures and subpanels is available on Zenodo at https://doi.org/10.5281/ZENODO.7875425[25].

## Data availability

The datasets used and/or analysed during the current study available from the corresponding author on reasonable request.

Received: 2 June 2023; Accepted: 25 June 2024
Published online: 06 August 2024

## References

1. Tran-Van-Minh, A. *et al.* Contribution of sublinear and supralinear dendritic integration to neuronal computations. *Front. Cell. Neurosci.*https://doi.org/10.3389/fncel.2015.00067 *(2015).*
2. Polsky, A., Mel, B. W. & Schiller, J. Computational subunits in thin dendrites of pyramidal cells. *Nat. Neurosci.* **7**, 621–627. https://doi.org/10.1038/nn1253 (2004).
3. Poirazi, P., Brannon, T. & Mel, B. W. Pyramidal neuron as two-layer neural network. *Neuron* **37**, 989–999. https://doi.org/10.1016/S0896-6273(03)00149-1 (2003).
4. Gidon, A. *et al.* Dendritic action potentials and computation in human layer 2/3 cortical neurons. *Science* **367**, 83–87. https://doi.org/10.1126/science.aax6239 (2020).
5. Xu, N.-L. *et al.* Nonlinear dendritic integration of sensory and motor input during an active sensing task. *Nature* **492**, 247–251. https://doi.org/10.1038/nature11601 (2012).
6. Wilson, D. E., Whitney, D. E., Scholl, B. & Fitzpatrick, D. Orientation selectivity and the functional clustering of synaptic inputs in primary visual cortex. *Nat. Neurosci.* **19**, 1003–1009. https://doi.org/10.1038/nn.4323 (2016).
7. Schmidt-Hieber, C. & Nolan, M. F. Synaptic integrative mechanisms for spatial cognition. *Nat. Neurosci.* **20**, 1483–1492. https://doi.org/10.1038/nn.4652 (2017).
8. Takahashi, N., Oertner, T. G., Hegemann, P. & Larkum, M. E. Active cortical dendrites modulate perception. *Science* **354**, 1587–1590. https://doi.org/10.1126/science.aah6066 (2016).
9. Abrahamsson, T., Cathala, L., Matsui, K., Shigemoto, R. & DiGregorio, D. A. Thin dendrites of cerebellar interneurons confer sublinear synaptic integration and a gradient of short-term plasticity. *Neuron* **73**, 1159–1172. https://doi.org/10.1016/j.neuron.2012.01.027 (2012).
10. Hu, H., Martina, M. & Jonas, P. Dendritic mechanisms underlying rapid synaptic activation of fast-spiking hippocampal interneurons. *Science* **327**, 52–58. https://doi.org/10.1126/science.1177876 (2010).
11. Tzilivaki, A., Kastellakis, G. & Poirazi, P. Challenging the point neuron dogma: FS basket cells as 2-stage nonlinear integrators. *Nat. Commun.* **10**, 3664. https://doi.org/10.1038/s41467-019-11537-7 (2019).
12. Cazé, R. D., Humphries, M. & Gutkin, B. Passive dendrites enable single neurons to compute linearly non-separable functions. *PLoS Comput. Biol.* **9**, e1002867. https://doi.org/10.1371/journal.pcbi.1002867 (2013).
13. Cazé, R., Humphries, M. & Gutkin, B. Spiking and saturating dendrites differentially expand single neuron computation capacity. In *Advances in Neural Information Processing Systems* (eds Pereira, F. *et al.*) (Curran Associates Inc., 2012).
14. Tran-Van-Minh, A., Abrahamsson, T., Cathala, L. & DiGregorio, D. A. Differential dendritic integration of synaptic potentials and calcium in cerebellar interneurons. *Neuron* **91**, 837–850. https://doi.org/10.1016/j.neuron.2016.07.029 (2016).
15. Tran-Van-Minh, A., Rebola, N., Hoehne, A. & DiGregorio, D. A. Two-photon neurotransmitter uncaging for the study of dendritic integration. In *Multiphoton Microscopy* (ed. Hartveit, E.) (Springer, 2019). https://doi.org/10.1007/978-1-4939-9702-2_3.
16. Scorcioni, R., Polavaram, S. & Ascoli, G. A. L-Measure: A web-accessible tool for the analysis, comparison and search of digital reconstructions of neuronal morphologies. *Nat. Protoc.* **3**, 866–876. https://doi.org/10.1038/nprot.2008.51 (2008).
17. Ujfalussy, B. B., Makara, J. K., Lengyel, M. & Branco, T. Global and multiplexed dendritic computations under in vivo-like conditions. *Neuron* **100**, 579-592.e5. https://doi.org/10.1016/j.neuron.2018.08.032 (2018).
18. Smith, S. L., Smith, I. T., Branco, T. & Häusser, M. Dendritic spikes enhance stimulus selectivity in cortical neurons in vivo. *Nature* **503**, 115–120. https://doi.org/10.1038/nature12600 (2013).
19. Palmer, L. M. *et al.* NMDA spikes enhance action potential generation during sensory input. *Nat. Neurosci.* **17**, 383–390. https://doi.org/10.1038/nn.3646 (2014).
20. Fischer, L. *et al.* Dendritic mechanisms for in vivo neural computations and behavior. *J. Neurosci.* **42**, 8460–8467. https://doi.org/10.1523/JNEUROSCI.1132-22.2022 (2022).
21. Malsburg, C. V. D. The what and why of binding: The modeler's perspective. *Neuron* **24**, 95–104. https://doi.org/10.1016/S0896-6273(00)80825-9 (1999).
22. Yu, X. & Lau, E. *The Binding Problem 2.0: Beyond Perceptual Features* (Wiley, 2023).
23. Losonczy, A. & Magee, J. C. Integrative properties of radial oblique dendrites in hippocampal CA1 pyramidal neurons. *Neuron* **50**, 291–307. https://doi.org/10.1016/j.neuron.2006.03.016 (2006).
24. Stimberg, M., Brette, R. & Goodman, D. F. Brian 2, an intuitive and efficient neural simulator. *elife* **8**, e47314. https://doi.org/10.7554/eLife.47314 (2019).
25. Caze, R. Demonstration that sublinear dendrites enable linearly non-separable computations, https://doi.org/10.5281/ZENODO.7875425 (2023).

## Acknowledgements

B.S.G. would like to acknowledges the support from the Basic Science Program Basic Research Program at the National Research University Higher School of Economics (HSE University). This work was partially supported by the ANR projects "CerebComp" and "InTempCode" to B.S.G. and D.A.D.

## Author contributions

R.C., A.T. and D.A.D. conceived the experiments, R.C., D.A.D. and B.S.G. conceived the theory, R.C. carried out the computational research A.T. conducted the experiments, R.C. and A.T. analysed the results, D.A.D, B.S.G and R.C. wrote the manuscript. All authors reviewed the manuscript.

## Competing interests

The authors declare no competing interests.

## Additional information

**Supplementary Information** The online version contains supplementary material available at https://doi.org/10.1038/s41598-024-65866-9.

**Correspondence** and requests for materials should be addressed to R.D.C., B.S.G. or D.A.D.

**Reprints and permissions information** is available at www.nature.com/reprints.

**Publisher's note** Springer Nature remains neutral with regard to jurisdictional claims in published maps and institutional affiliations.

**Open Access** This article is licensed under a Creative Commons Attribution-NonCommercial-NoDerivatives 4.0 International License, which permits any non-commercial use, sharing, distribution and reproduction in any medium or format, as long as you give appropriate credit to the original author(s) and the source, provide a link to the Creative Commons licence, and indicate if you modified the licensed material. You do not have permission under this licence to share adapted material derived from this article or parts of it. The images or other third party material in this article are included in the article's Creative Commons licence, unless indicated otherwise in a credit line to the material. If material is not included in the article's Creative Commons licence and your intended use is not permitted by statutory regulation or exceeds the permitted use, you will need to obtain permission directly from the copyright holder. To view a copy of this licence, visit http://creativecommons.org/licenses/by-nc-nd/4.0/.

© The Author(s) 2024